PCCP

Gas-phase oxidation and nanoparticle formation in multi-element laser ablation plumes

Journal:	*Physical Chemistry Chemical Physics*
Manuscript ID	CP-ART-05-2022-002437.R1
Article Type:	Paper
Date Submitted by the Author:	03-Oct-2022
Complete List of Authors:	Kautz, Elizabeth; Pacific Northwest National Laboratory, National Security Directorate Zelenyuk, Alla; Pacific Northwest National Laboratory Gwalani, Bharat; Pacific Northwest National Laboratory; North Carolina State University at Raleigh, Materials Science and Engineering Phillips, Mark; University of Arizona, Optics Science Center; Opticslah; Pacific Northwest National Laboratory, National Security Directorate Harilal, Sivanandan; Pacific Northwest National Laboratory; Washington State University, Chemistry

PCCP

ARTICLE TYPE

Cite this: DOI: 00.0000/xxxxxxxxxx

Gas-phase oxidation and nanoparticle formation in multi-element laser ablation plumes

Elizabeth J. Kautz,[a] Alla Zelenyuk,[a] Bharat Gwalani,[ab] Mark C. Phillips,[c] and Sivanandan S. Harilal*[ad]

Received Date
Accepted Date

DOI: 00.0000/xxxxxxxxxx

The evolution from gas-phase oxidation to nanoparticle and agglomerate formation was studied in nanosecond laser-produced plasmas of a multi-principal element alloy target in air. Gas-phase oxidation of plasma species was monitored in-situ via optical emission spectroscopy, while a custom-built single particle mass spectrometer was used to measure size and compositions of agglomerated nanoparticles formed in laser ablation plumes. Ex-situ analysis employing transmission electron microscopy was used to study nanoparticle morphology, crystal structure, and element distribution at the nanoscale. Emission spectra indicate that gas-phase oxidation of elements in the alloy target are formed at varying times during plume evolution, and mass spectrometry results indicate fractal agglomerates contain all principal alloying elements and their oxides. Finally, electron microscopy characterization illustrates that these agglomerates consist of multiple material types: sub-10 nm diameter amorphous, multi-element nanoparticles, ≈ 10-30 nm diameter Ti-rich crystalline oxide nanoparticles, and ejected base material. Results highlight that the multi-component target composition impacts molecular formation in the gas phase and the morphology, composition, and structure of nanoparticles and agglomerates formed.

1 Introduction

Laser produced plasmas (LPPs) are highly resource efficient, repeatable, tunable, lab-scale test beds for studying chemical reactions occurring in plasmas or fireballs produced from detonation of energetic materials, and nanoparticle (NP) generation.[1,2] The generation of a LPP involves focusing a laser beam onto a target, resulting in material removal and generation of a plasma. When a laser ablation (LA) plume expands into a background gas, rapid plasma cooling occurs due to collisions with ambient gas species. The initial temperature and density of the LPP, as well as ambient pressure and composition, define the timescales for plasma cooling. In a reactive background gas, such as air or oxygen (O_2), the progression of atoms and ions to monoxides, higher oxides, NPs, and agglomerates occurs with increasing time after plasma onset. Molecular formation in LPPs is favored farther from the target at the cooler plasma periphery, at temperatures ≈ 8000 K or less.[1] At later times, NPs nucleate, grow, and coalesce, forming fractal NP agglomerates. While molecular and NP formation in LA plumes has been explored previously,[3–9] limited experimental work has been able to characterize gas to solid phase processes in bi- and multi-element LA plumes.[10] In part, this gap is due to the challenging nature of tracking the progression from ions and atoms, diatoms, larger molecules, aerosols, and finally particulates, which requires multiple complementary techniques that together cover several orders of magnitude in time.[11]

NPs are studied in numerous application areas from understanding debris formation in an explosion event to nanotechnology-based applications such as catalysis, electronics, sensing, and batteries.[12] The unique properties possible with NPs have led to a growing interest in physical and chemical synthesis routes, such as physical/chemical vapor deposition, sol-gel, inductively coupled plasmas, and pulsed LA.[13,14] Among these, pulsed LA is a straightforward, attractive method for NP synthesis due to the vast parametric space (e.g., laser wavelength, pulse energy, width, frequency, focusing conditions) that can be leveraged for tuning NP size, composition, structure, and properties.[15,16] However, fundamental mechanisms including the thermo- and plasma-chemical reactions routes and factors contributing to NP formation are still not well understood, particularly for vapor-phase synthesis routes in reactive gaseous environments. Yet, these reaction routes are crucial for developing and generating NPs with desired properties and functionalities, in addition to understanding debris formation in a fireball scenario, and hence re-

[a] Pacific Northwest National Laboratory, Richland, WA 99352, USA
[b] Department of Materials Science and Engineering, North Carolina State University, Raleigh, NC 27606, USA
[c] James C. Wyant College of Optical Sciences, University of Arizona, Tucson, Arizona 85721, USA
[d] Department of Chemistry, Washington State University, Pullman, WA 99164, USA
* Corresponding authors: hari@pnnl.gov

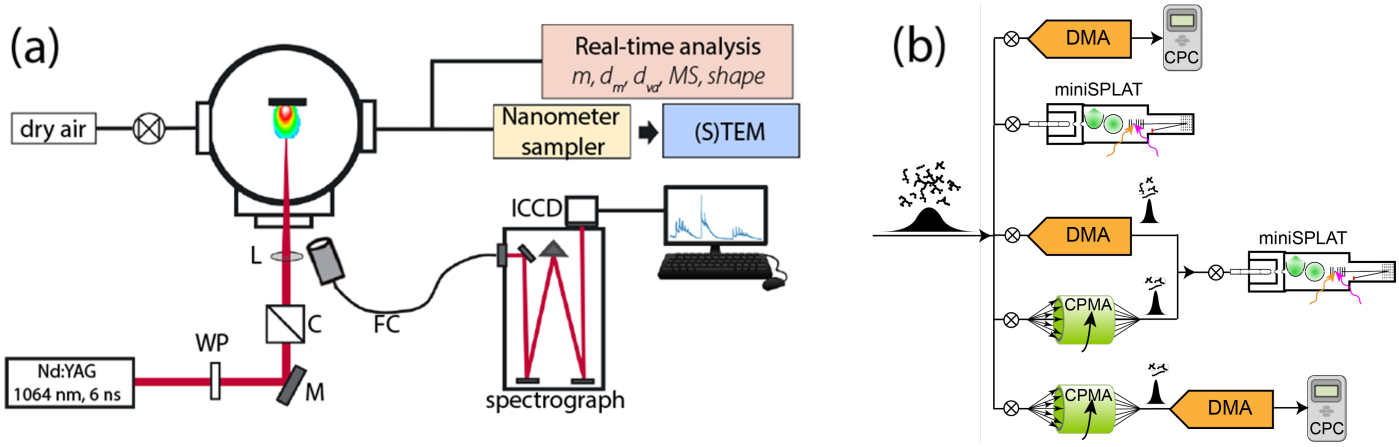

Fig. 1 (a) Experimental workflow for LPP and NP generation, and characterization, including ns LA using a Nd:YAG laser, real-time and (S)TEM analysis. Parameters obtained in real-time analysis (detailed in sub-figure b) include: m (mass), d_m (mobility diameter), d_{va} (vacuum aerodynamic diameter), MS (mass spectrum), and shape. Acronyms used in the schematic are defined as follows: WP (wave plate), M (mirror), C (cube polarizer), L (lens), FC (fiber cable), ICCD (intensified charged coupled device), STEM (Scanning Transmission Electron Microscopy). (b) Schematic of different pathways for real-time analysis, including the following components: DMA (differential mobility analyzer), CPC (condensation particle counter), miniSPLAT (a single particle mass spectrometer), and CPMA (centrifugal particle mass analyzer).

quire further study.

Here, a LPP system is used to understand gas-phase oxidation that may occur at certain spatial locations and/or times in a high explosion (HE) event. Atoms and ions exist in the high-temperature LPP at early times after its formation. LPP expansion and interaction with the ambient gas medium lead to plasma cooling and lower temperatures that favor gas-phase oxidation reactions, followed by subsequent NP nucleation, growth, and agglomeration. We use multiple diagnostics to understand molecular formation routes (e.g., gas-phase oxidation) and how particulate materials (i.e., NPs and NP agglomerates) are formed in multi-element LPPs. We track particulate formation in multi-element plasma plumes in atmospheric pressure air from gas to solid phases via: gas-phase optical emission spectroscopy (OES), Scanning Mobility Particle Sizer (SMPS), single particle mass spectrometry, and electron microscopy. A refractory-based high entropy alloy (RHEA) containing 10 % Al, 30 % Ti, 20 % Zr, 20 % Nb, 15 % Ta, 5 % V (in at. %)[17] was selected as a model system for the present study that is comprised of several elements that undergo different thermo- and plasma-chemical reactions in an oxygen-containing environment. This system presents a case study relevant to applications including explosion monitoring, pulsed laser deposition, and additive manufacturing, in which multi-element or high entropy NPs are formed.

2 Experimental materials and methods

The experimental set-up used for generating LPPs and NPs and associated characterization is shown in Figure 1. For plasma generation, a Nd:YAG laser was used with 1064 nm wavelength, ≈6 ns FWHM, operated at 10 Hz, with a laser fluence of ≈20 J/cm^2. These laser parameters were selected to generate a plasma that undergoes plume chemistry similar to a detonation event. In ns LA, plume chemistry (i.e., gas-phase oxidation) typically occurs at later times in plasma evolution when the plasma temperature is ≈8000 K or lower.[1]

The alloy target was mounted inside a small chamber onto a stage for spectroscopic analysis and NP generation. Details regarding target fabrication are detailed in Supplementary Information Appendix S1. The stage was placed on a x-y translator to prevent drilling. LPPs were generated in a 1 atm pressure flowing dry air environment (with a flow rate of 5 L/min). For recording spatially integrated spectral features, light emitted from the plasma was collected with a lens and focused to a 400 μm multimode fiber coupled to a 0.5 m spectrograph (Acton Spectrapro 2500i) equipped with an intensified charged coupled device (ICCD, Princeton Instruments PIMAX4). A 1200 grooves per mm grating was used for all spectral measurements with a spectral resolution of ≈ 0.080 nm, measured using a 632 nm He–Ne laser.

Mobility diameter (d_m) size distributions of LA-generated particles were obtained using a SMPS, comprised of a differential mobility analyzer (DMA, Model 3081, TSI Inc.) and a condensation particle counter (CPC, Model 3786, TSI Inc). In order to minimize coagulation of particles during transport and analysis, the SMPS was located in close vicinity to the LA cell; this close proximity limited particle transport time to ≈1-3 s. Mass spectra and vacuum aerodynamic diameters (d_{va}) of individual LA-generated particles were measured with miniSPLAT, a single particle mass spectrometer.[18,19] For the miniSPLAT measurements, LA-generated particles were first introduced into a 100 L Teflon sampling chamber, where they were diluted with dry air by a factor of ≈10 to minimize particle coagulation. miniSPLAT was also used to characterize size and mass-selected particles classified by a DMA and a centrifugal particle mass analyzer (CPMA, Cambustion), respectively. Similarly, SMPS was used to measure d_m size distributions of mass-selected particles. Combined, these measurements yield information on fractal dimension of NP agglomerates and their effective densities. For the materials with known densities these measurements also yield average diameter of primary NP, number of primary NPs, void fraction and dynamic

shape factors as a function of particle mass or size.[19]

NPs and NP agglomerates were characterized via TEM by depositing them on Lacey Formvar/Carbon mesh copper grids using a Nanometer Aerosol Sampler (Model 3089, TSI Inc) for 5 minutes at a sampling flow rate of 1 L/min. Analysis was performed using a probe-corrected FEI Titan 80–300 STEM instrument operated at 300 kV. Scanning TEM, (S)TEM, mode with a high-angle annular dark-field (HAADF) detector and Aztec's energy dispersive spectroscopy (EDS) data collection and analysis system for compositional analysis were used.

3 Results

Excitation temperature and electron density could not reliably be determined for the plasmas produced from the alloy target given the extremely congested spectral features and numerous overlapping transitions due to the multiple elements contributed to emission spectra. For comparison, we determined physical conditions for a pure Al sample under the same LA conditions to understand temperature, cooling rates, and densities. The early time physical conditions for a pure Al target were determined via time-resolved emission spectra.[20,21] The Al target was selected for these measurements given ionic and molecular lines are well characterized in literature, and Al is present in the alloy. Temperatures were estimated using the ratio of Al II transitions at 281.62 and 263.15 nm, and temperatures at later times ($\geq$ 5 μs) were measured using the PGOPHER simulation tool for the (0,1) AlO band, with the strongest band head at $\approx$508 nm.[22] Excitation temperature was $\approx$13,600 K at 1.5 μs, and by 3 μs the temperature decreased to $\approx$11,500 K. At 5 μs, the temperature was $\approx$4,250 K, and by 110 μs it dropped to $\approx$2,800 K. AlO formation was found to be favorable between 4250 - 2500 K from $\approx$5 - 110 μs. These temperature values correspond to approximate cooling rates of $\approx 8.6 \times 10^8$ K/s from 1.5 - 3 μs), $\approx 2 \times 10^7$ K/s from 5 - 10 μs), and $\approx 1 \times 10^7$ K/s from 90 - 100 μs).[20] These rates are estimated from spatially-integrated spectral data, and can vary with space and time due to the heterogeneous nature of LPPs.[23,24] We also recognize that the plasma physical conditions vary with target properties,[25] composition, and microstructure, in addition to shock physics, plasma chemistry, and reaction mechanisms.[10] We can expect the temperature of the multi-component system to be different than single element plasmas, $\pm$10 %, based on results reported elsewhere.[10,25]

OES is a useful tool for tracking the evolution of plasma species from ions and atoms to diatoms and higher oxides.[1,21] Time-resolved emission spectral features for a broad wavelength range (400 - 730 nm) are reported in Figure 2. Spectral features are dominated by atomic emission at early times (i.e., 5 μs). By 30 μs, strong atomic emission is still observed, with weak emission from molecular bands in the wavelength range of $\approx$ 500 - 730 nm. At 50 μs, emission from molecules is prominent, and a strong background-like emission feature is present. This relative emission signatures from molecules becomes stronger by 70 μs, where the emission from atoms is weak. The appearance of background like broadband signal at later times of plasma evolution can be attributed to emission from oxide molecules of heavier elements, such as Ti, Zr, Nb, Ta, and V, which cannot be resolved with the spectrograph system used here.[1] Thermal emission from NPs can also contribute.

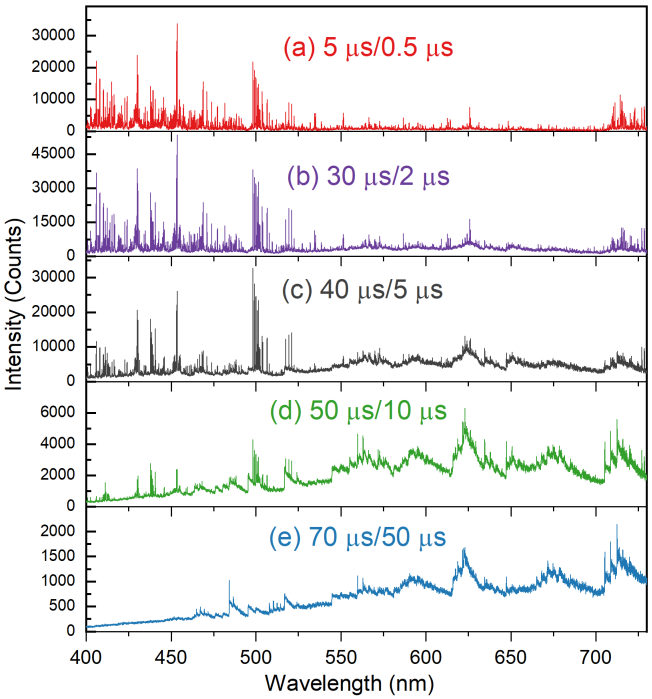

Fig. 2 Optical emission spectra for plasmas produced via LA of the RHEA target collected over the range of 400 - 730 nm for varying times after plasma onset. Gate delay/width are noted on each sub-figure, and are as follows: (a) 5 μs/0.5 μs, (b) 30 μs/2 μs, (c) 40 μs/5 μs, (d) 50 μs/10 μs, and (e) 70 μs/50 μs.

To further understand major species contributing to emission spectral features, alloy spectra were compared to those collected from pure metal targets at 30 μs and 70 μs after plasma onset when molecular emission features become strong (Figure 3). In each sub-figure, prominent molecular bands are highlighted and labelled.[26] Some broad molecular emission bands could be from higher oxides, which are even more sparsely reported in literature in comparison to monoxides. At 30 μs after plasma onset, the alloy target shows good agreement with Ti and Zr spectra in the $\approx$ 550-725 nm region, and agreement with Nb spectra in the 630-680 nm range. We attribute broad peaks in the alloy spectrum at $\approx$560, 590, 625 nm, and 675 to TiO, and $\approx$ 650 nm to ZrO at 30 μs (Figure 3(a)). Spectral features similar to NbO were observed at $\approx$650, 660 nm and 675 nm in the alloy spectrum (Figure 3(b)). NbO and ZrO emission may contribute to the broad band at $\approx$650 nm. To the best of the authors' knowledge, bands at 660 and 675 nm for NbO are not documented in literature. At later times (70 μs), TiO spectral signatures are prominent, particularly in the $\approx$ 550-700 nm range. In addition, AlO bands are observed from $\approx$ 460-530 nm. From Figure 3, we find that Ti, Zr, and Nb molecular emission spectral features are present at earlier times in plasma evolution, and TiO persists until later times when AlO is also prominent. VO bands were not observed, likely because of the low concentration ($\approx$ 5 at% V in the base alloy). TaO bands were also not observed in the given spectral range (where some strong TaO bands have been reported at 415.54 nm, 481.04

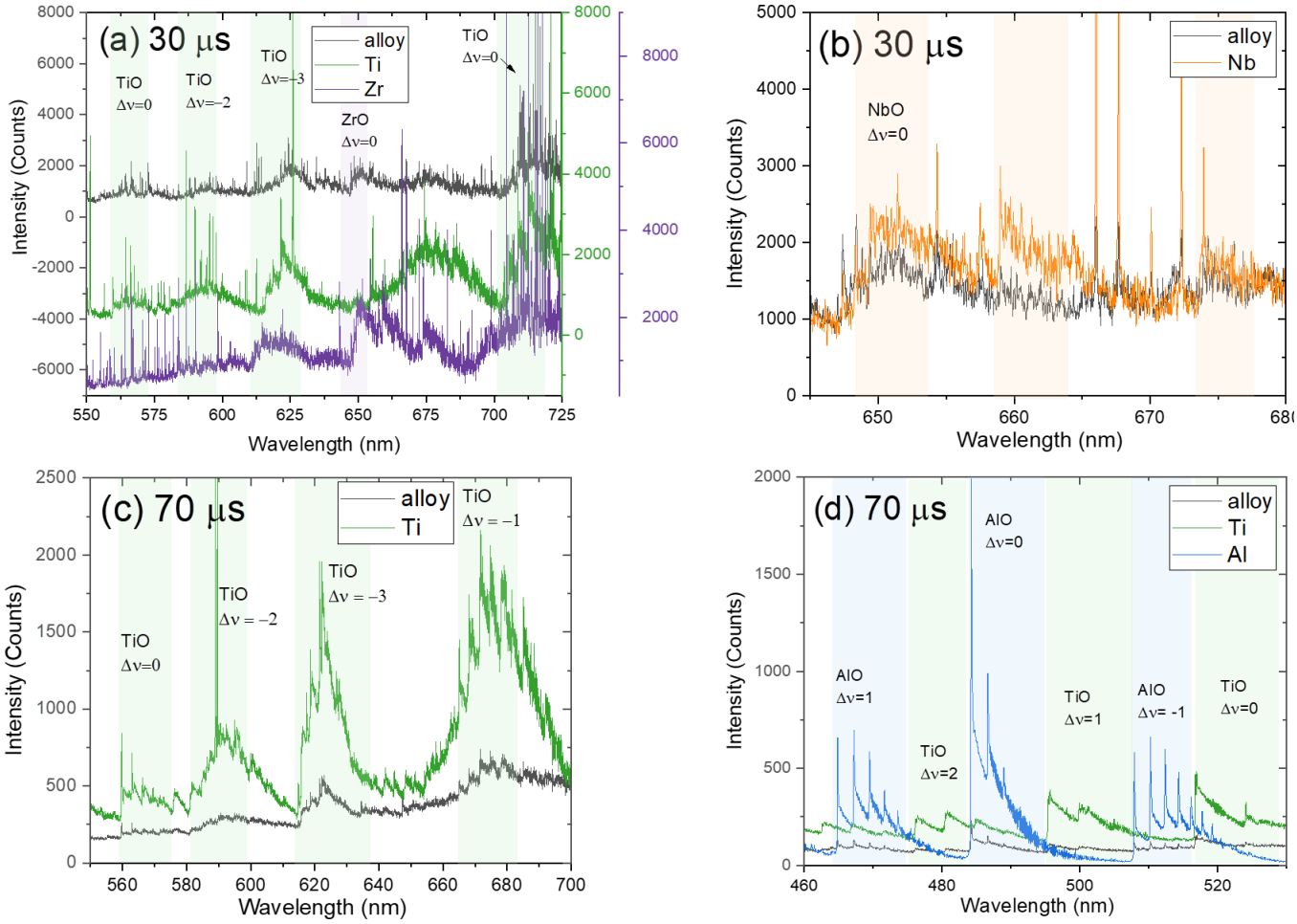

Fig. 3 Select emission spectra for (a,b) 30 μs/2 μs and (c,d) 70 μs/50 μs gate delays/widths.

nm, and 556.70 nm).[26] The lack of clear TaO signatures may be related to the fact that TaO has reduced persistence in the plasma relative to other molecular species.[20] TaO is also known to form higher oxides readily, which could contribute to the strong broadband emission signal in alloy spectra at times $\geq$ 50 μs.[20]

While OES is useful for tracking atoms and diatoms, its use is limited for tracking larger molecules and NPs. Hence, we characterized physico-chemical properties of LA-generated particulates (i.e., NP agglomerates) by SMPS and miniSPLAT. Results from real-time characterization of LA-produced particulates are presented in Figures 4 and 5. Normalized mobility (d_m) and vacuum aerodynamic diameter (d_{va}) size distributions are given in Figure 4(a). These results show that the width of the d_{va} size distribution is significantly narrower than that of d_m, which indicates the fractal morphology of the LA-generated NP agglomerates with d_{va} that are nearly independent of their mass and d_m,[19] as illustrated in Figure 5(a). The simultaneous measurements of particle d_{va} and d_m yield measurements of particle effective density, ρ_{eff}. Figure 5(b) shows that the effective density decreases rapidly with increased d_m, with a slope that yields fractal dimension of $D_{fa} \approx 2$, indicative of fractal agglomerates. The values of effective densities are significantly lower than the material density of the alloy (7.4 g/cm^3), consistent with a small size of primary NP and large size-dependent void fraction of NP agglomerates.

The Figure 4(a) inset presents the mass-d_m relationship, derived from the SMPS-measured d_m distributions of mass-selected particles shown in Figure 5(c), that makes it possible to calculate mass of ablated material. In addition, the slope of the mass-d_m relationship D_{fm}=1.92 is indicative of fractal morphology of NP agglomerates, where D_{fm}=3 is for compact particles, D_{fm}=2 is for perfect fractal agglomerates, and D_{fm}=1 is for infinite linear chains.[19] The average mass spectrum of all characterized NP agglomerates, shown in Figure 4(b), contains mass spectral peaks from all elements and their oxides. To examine potential differences between compositions of individual particles, 4305 individual particle mass spectra (IPMS) acquired in this study were classified using K-mean clustering approach into classes that contain particles with very similar mass spectra.[27] This classification process yielded 2 distinct particle classes: Class 1 and Class 2, which contain 61% and 39% of total IPMS, respectively. Figure S2 shows the average mass spectra of Class 1 and Class 2 plotted on linear (a) and logarithmic (b) scales for relative mass spectral intensities. The comparison of Class 1 and Class 2 indicates that particles classified into Class 2 contain relatively larger fraction of oxidized species.

The average mass spectrum (Figure 4(b)) also shows that peak

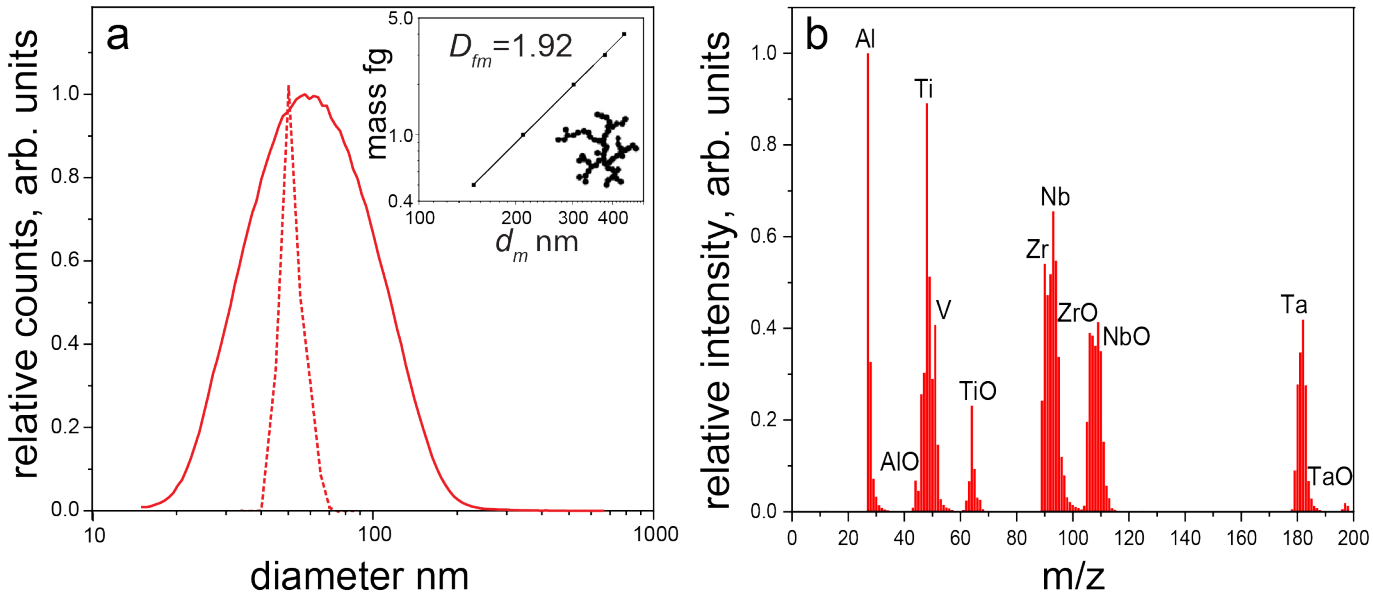

Fig. 4 Results from real-time particulate characterization via SMPS and miniSPLAT. (a) Normalized mobility (d_m - solid line) and vacuum aerodynamic diameter (d_{va} - dashed line) size distributions. Inset: measured mass-d_m relationship. (b) Average mass spectrum of all particles analyzed.

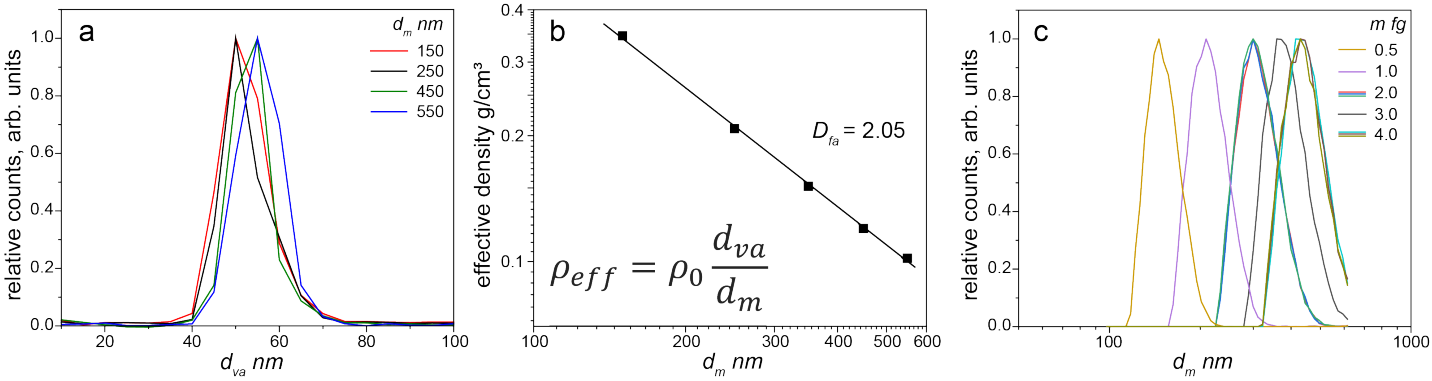

Fig. 5 Results from real-time particulate characterization: (a) Vacuum aerodynamic diameter size distributions of mobility-selected particles, which are used to calculate particle effective density as a function of their mobility diameter (d_m); (b) Plot of the calculated effective density as a function of d_m, displayed in a log-log domain, showing power law relationship. This relationship is used to determine fractal dimension of NP agglomerates (D_{fa}) shown on the plot; (c) Mobility diameter size distributions of mass-selected particles. The relationship between particle mass and d_m is shown in Figure 4(a) (inset). Note that for ease of comparison all size distributions were normalized to the same maximum peak height.

intensities for ZrO, NbO, and TiO are higher than those observed for oxides of Al, Ta, and V, consistent with OES that suggests TiO, ZrO, and NbO are predominant in the plasma due to higher number density compared to other species. It should also be noted that the detection efficiency for lower m/z values is better than for higher m/z, hence the Al^{+1} signal at ≈ 27 Da appears strong, despite the relatively low concentration of Al in the alloy (10 at. %).

A low magnification bright-field image (Figure 6) shows the fractal morphology of NP agglomerates, consistent with their real-time analysis. Numerous sub-10 nm NPs are observed in addition to more sparsely located larger particles, with ≈ 10-30 nm in diameter. Further evidence of NP agglomeration and morphology is given in Supplemental Information Figure S1. To identify the structure and composition of the NPs within the fractal agglomerates shown in Figure 6, we characterized select NPs in detail via (S)TEM, with results reported in Figure 7. In addition to NPs and agglomerates previously observed in Figure 7, we also find ejected target material (Figure 7(a)) with the same constituent phases as the starting alloy microstructure detailed in Supplemental Information Figure S3.

Based on STEM-EDS maps in Figure 7(c)-(j), the smaller, sub-10 nm NPs contain signals from all constituent elements (i.e., Al, Ti, Zr, Nb, Ta, and V) and O. These NPs are structurally amorphous as shown in Figure 7(k). A larger (≈20 nm) NP is also observed in Figure 7(a). A similar NP given in Figure 7(b) appears to have stronger Ti and O signals relative to other elements (see Figure 7(i)-(j)). The white arrow in Figure 7(i) indicates this Ti-enriched NP. This NP has a crystalline, face centered cubic (FCC) structure as shown in Figure 7(k) with stacking faults. This larger NP can be based on the TiO_2 structure given the FCC structure, the presence of stacking faults (previously observed during solid-

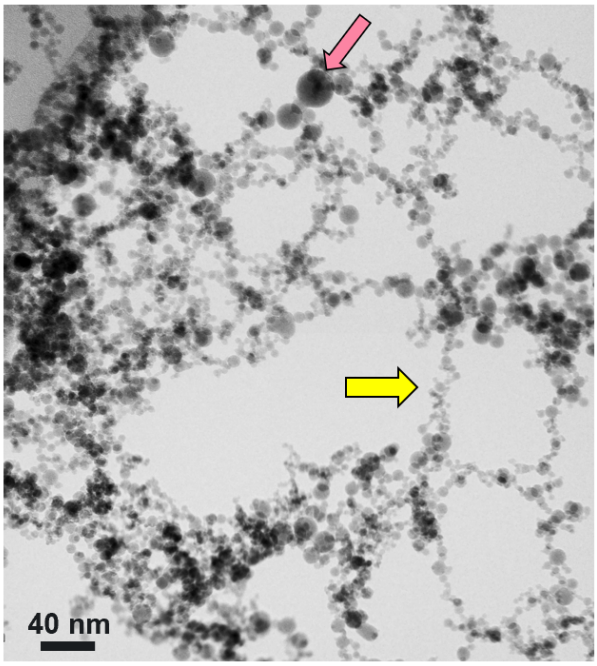

Fig. 6 Bright field (BF)-TEM results showing fractal NPs generated via laser ablation of the refractory-based alloy target in air. A pink arrow points towards an example of a larger NP, and a yellow arrow points towards smaller, agglomerated NPs.

ification or deformation in TiO_2 [28,29]), and the stronger Ti and O signals in this region. Larger features (≈ 50 nm) also observed in Figure 7(a) were found to have a similar crystal structure as the base alloy which consists of nanodomains of ordered and disordered B2 + BCC phases. This structure is similar to the base alloy (detailed in Supplemental Information Figure S3), suggesting that some target material was not fully vaporized in the plasma generation process.

4 Discussion

NP formation mechanisms in LA plumes depend on several factors, including plasma- and thermo-chemical reactions that occur as the plasma expands into the surrounding environment, nature of environment (gas or liquid), ablation mechanisms, and target material properties. The thermo- and plasma-chemical reactions that take place are dictated by the plasma properties (i.e., temperature and particle density) and LPP generation parameters, including laser power, wavelength and pulse duration. [30–32] Owing to the highly transient and heterogeneous nature of LPPs, which for ns LA is also influenced by significant laser-plasma interaction, plasma properties, and chemistry evolution are known to vary with both space and time. [1]

The evolution of alloy spectral features (Figure 2) demonstrates that gas-phase oxidation and molecular formation in LPPs occur as the plasma expands and interacts with the ambient air. This molecular formation is strongly dependent on plasma physical conditions which are favorable for the formation of oxide molecules at different times after plasma onset depending on thermodynamic properties and kinetics. Molecular formation in LPPs typically occurs when plasma temperatures have reached on the order of 8000 K or less, [1] which is estimated to occur ≈ 4-5 μs after onset. The good agreement of alloy emission spectral features with spectra from pure Ti, Zr, and Nb plasmas at ≈ 30 μs, and Ti and Al spectral features at later times (i.e., 70 μs) suggests that molecular formation occurs at different temperatures, and hence times, after plasma onset depending on the system. [20] These findings are consistent with the concept that free energies of diatom formation are minimum at different temperatures according to data reported in the NIST JANAF tables, when considering temperatures between 1000 - 6000 K. [33] For instance, ΔG_f is minimum for AlO at ≈ 2800 K in comparison to 3600 K for TiO, 4700 K for ZrO, 5000 K for NbO, and 6000 K for TaO. [33] Hence, AlO and TiO signals may be strong at later times after plasma onset (Figure 3(c)-(d)) in part since AlO and TiO are thermodynamically stable at the lower temperatures when compared to ZrO and NbO. The tendency for diatoms to be consumed in the formation of higher oxides, and the numerous possible reaction routes for all plasma species also contribute to the reaction products that can form beyond monoxides/diatoms. [1] Some of the broad spectral features given in Figure 3 may be attributed to higher oxides such as TiO_2, ZrO_2, NbO_2, etc.

As the plasma cools rapidly in air, NPs nucleate when the supersaturated vapor phase becomes unstable relative to the solid phase. After nucleation, NPs grow, but the extent of growth is dictated by environmental parameters (e.g., temperature). [34] The majority of NPs formed via LA of the refractory-based alloy are amorphous with diameters of ≤ 10 nm. This rapid cooling can prevent atomic arrangement into a crystalline structure and limits particle growth. The background air pressure of 1 atm also contributes to plume confinement and therefore increased collisions of plume species with the background gas (and hence gas-phase oxidation), and NP agglomeration. [15,35] Another key parameter contributing to the dimensions of NP fractal agglomerates is the air flow rate; higher flow rates were shown to reduce agglomeration. [19]

Due to the reactivity of plasma species with oxygen, and the formation of molecular species that occur before particle nucleation, the sub-10 nm amorphous NPs produced are composed of all principal alloying elements and oxygen, as illustrated in by the STEM results (Figures 7). Mass spectrometry results (Figure 4 and Figure S2) highlight that agglomerates of these NPs contain signals from all principal alloying elements and oxides. While the mass spectrometry results could not unambiguously determine the composition of individual NPs in the agglomerates, they do highlight that some particles contain a relatively large fraction of oxidized species, suggesting these were formed at lower plasma temperatures, either at later times and/or at the periphery of plasma plume. While signal in STEM-EDS maps from sub-10 nm NPs is relatively low given their small size and the presence of multiple principal alloying elements, the qualitative assessment that multiple elements contribute to these amorphous NPs is clear. It should also be noted that there may be projection artefacts that are unavoidable in which signals from overlapping NPs contribute to the STEM-EDS maps. To quantitatively detail composition of NPs and agglomerates, a higher-resolution technique such as atom probe tomography (APT) should be employed. Mapping

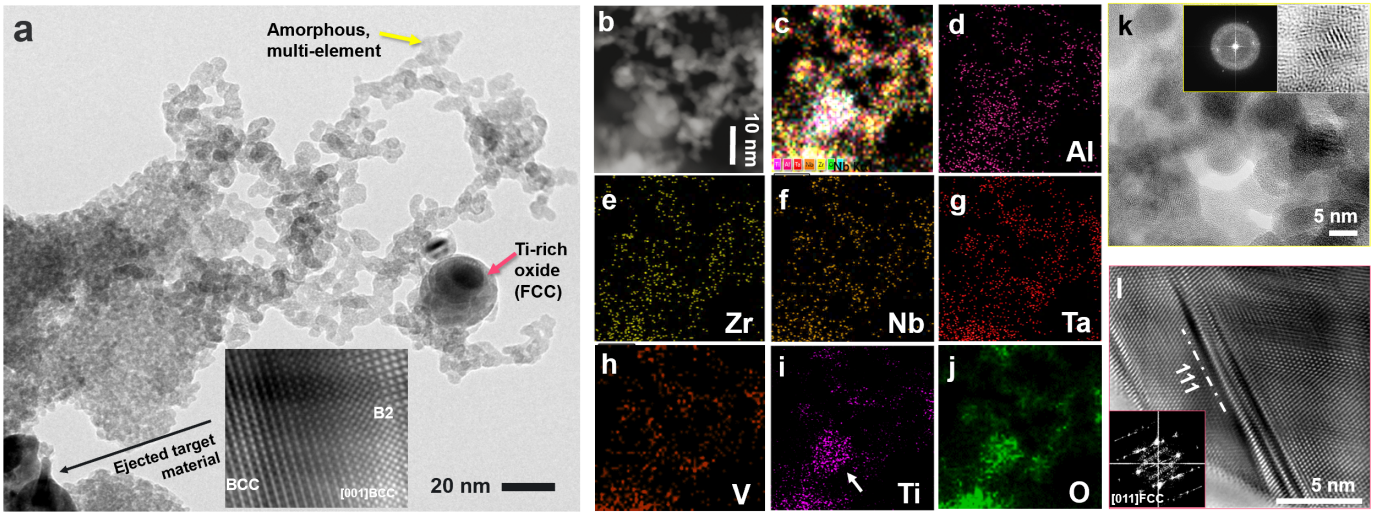

Fig. 7 Characterization of NPs using (S)TEM. (a) BF-TEM image of fractal multi-principal element oxide NPs with an amorphous structure, larger Ti-rich oxide (crystalline) NPs, and ejected base material. (b) STEM image of NPs, and corresponding STEM-EDS maps for: (c) all principal alloying elements and oxygen, and individual maps of (d) Al, (e) Zr, (f) Nv, (g), Ta, (h) V, (i) Ti, and (j) O. (d)-(j) individual maps of Al, Zr, Nb, Ta, V, Ti, and O. The white arrow in (i) indicates a region of Ti enrichment. (k) TEM image with FFT and HR-TEM insets showing amorphous structure with a localized short-range ordering of atoms. (l) HR-TEM image of a Ti-rich NP, with an FFT of the image depicting the faulted FCC structure.

individual NP compositions in three dimensions via APT may be possible with advanced sample preparation methodologies.[36]

In addition to these agglomerated, sub-10 nm amorphous NPs, ≈10-30 nm diameter NPs are also formed in LPPs. Several of these are observed in Figure 6, and one is analyzed in more detail in Figure 7. Ejected base material is also observed from results reported in Figure 7. The observation of ejected base material indicates that not all the ablated material was vaporized, which is consistent with different ablation mechanisms contributing, such as normal boiling and phase explosion (i.e., explosive boiling).[37] We hypothesize that the sub-10 nm NPs were formed via homogeneous nucleation and grew from a supersaturated vapor-phase.[3,7] After nucleation of these NPs, reaction of vapor-phase molecules with nucleated particles lead to growth. Given several NPs characterized in this work are $<$ 10 nm in diameter, growth was likely limited by the rapid cooling in the 1 atm flowing air environment. This rapid cooling allowed for NPs to be amorphous, and entropic stabilization contributed to formation of multi-element NPs.

The larger FCC structured NPs with ≈ 10-30 nm diameter (Ti-rich) are more scarcely observed. We believe these to be Ti oxide NPs based on the identification of their FCC structure, consistent with TiO_2, and Ti enrichment observed via STEM-EDS mapping. However, conclusive identification of the composition of these NPs is not currently possible, and as mentioned previously, higher resolution techniques are required for identifying their stoichiometry. These NPs may have formed via heterogeneous nucleation, at different regions of the plasma plume in comparison to the smaller amorphous NPs. The nucleation of Ti oxide NPs likely took place when and where cooling rates were slower, allowing for more time for crystalline order to be established and the NPs to grow. The observed stacking faults (Figure 7(l)) likely originated during early crystal growth, as previously reported in the TiO_2 system.[28,38] Cooling rates are slower and plasma temperatures are lower at later times in plasma expansion and at the periphery. The strong TiO emission signal observed in emission spectra at later times (i.e., 70 μs as shown in Figure 3(c)-(d)) indicates that Ti oxides have greater persistence in the LPPs, and are hence prominent at later times, which suggests these Ti oxide molecules could serve as precursors for higher oxides and the crystalline Ti oxide NPs observed in Figure 7. In addition to this strong Ti oxide persistence demonstrated via OES, we also observed strong Al oxide molecular signatures at later times, however we did not observe any Al-rich, crystalline NPs in this work. No clear evidence of Al-rich oxide NPs could be due to several factors, including the fact that limited NPs were analyzed via STEM, and Al concentration in the target material is much less (10 at. %) in comparison to Ti (30 at. %). Further studies employing high resolution microscopy are needed to conclusively identify composition and structure of several NPs to better understand the phases formed in these multi-element LPPs.

5 Conclusion

In conclusion, the evolution from atoms to diatoms, molecules, NPs, and agglomerates in a reactive, multi-element LPP was studied. We found that molecular formation occurs at different timescales for different diatoms; ZrO, NbO and TiO are formed at earlier times after plasma onset in comparison to AlO. In addition, AlO and TiO persist for longer times when plasma temperatures are lower. Sub-10 nm diameter amorphous NPs containing all elements were formed via condensation from a supersaturated vapor phase, effectively forming so-called high entropy oxide NPs.[39] Larger ≈20-30 nm crystalline Ti oxide NPs were also observed, and likely nucleated at later times after plasma onset. The work reported here combines a wide range of in-situ and ex-situ diagnostics to track NP formation at various length and time scales in LA plumes, providing mechanistic insights into their formation in a multi-element system.

Conflicts of interest

Mark C. Phillips is a part-time employee of a small business.

Acknowledgements

This work was supported by the DOE/NNSA Office of Defense Nuclear Nonproliferation Research and Development (DNN R&D) and by the U.S. Department of Defense, Defense Threat Reduction Agency (DTRA; Contract No. HDTRA1-20-2-0001). Pacific Northwest National Laboratory is a multi-program national laboratory operated by Battelle for the U.S. Department of Energy under Contract DE-AC05-76RL01830.

Notes and references

1 E. J. Kautz, E. N. Weerakkody, M. S. Finko, D. Curreli, B. Koroglu, T. P. Rose, D. G. Weisz, J. C. Crowhurst, H. B. Radousky, M. DeMagistris *et al.*, *Spectrochimica Acta Part B: Atomic Spectroscopy*, 2021, 106283.

2 C. Kimblin, R. Trainham, G. A. Capelle, X. Mao and R. E. Russo, *AIP Adv.*, 2017, **7**, 095208.

3 R. Wood, J. Leboeuf, K.-R. Chen, D. Geohegan and A. Puretzky, *Applied surface science*, 1998, **127**, 151–158.

4 E. Lescoute, L. Hallo, D. Hébert, B. Chimier, B. Etchessahar, V. Tikhonchuk, J.-M. Chevalier and P. Combis, *Physics of Plasmas*, 2008, **15**, 063507.

5 S. Noël, J. Hermann and T. Itina, *Applied Surface Science*, 2007, **253**, 6310–6315.

6 B. Koroglu, M. Finko, C. Saggese, S. Wagnon, S. Foster, D. McGuffin, D. Lucas, T. P. Rose, J. C. Crowhurst, D. G. Weisz *et al.*, *Journal of Aerosol Science*, 2022, **162**, 105959.

7 M. S. Tillack, D. W. Blair and S. S. Harilal, *Nanotechnology*, 2004, **15**, 390–403.

8 M. Girault, L. Hallo, L. Lavisse, M. M. de Lucas, D. Hébert, V. Potin and J.-M. Jouvard, *Applied surface science*, 2012, **258**, 9461–9465.

9 M. Dell'Aglio, R. Gaudiuso, R. ElRashedy, O. De Pascale, G. Palazzo and A. De Giacomo, *Physical Chemistry Chemical Physics*, 2013, **15**, 20868–20875.

10 E. R. Wainwright, F. De Lucia, T. P. Weihs and J. L. Gottfried, *Spectrochimica Acta Part B: Atomic Spectroscopy*, 2021, 106270.

11 M. M. Modena, B. Rühle, T. P. Burg and S. Wuttke, *Advanced Materials*, 2019, **31**, 1901556.

12 S. Wang and L. Gao, *Industrial Applications of Nanomaterials*, Elsevier, 2019, pp. 181–203.

13 M. T. Swihart, *Current opinion in colloid & interface science*, 2003, **8**, 127–133.

14 A. Bapat, C. R. Perrey, S. A. Campbell, C. Barry Carter and U. Kortshagen, *Journal of Applied Physics*, 2003, **94**, 1969–1974.

15 M. Ullmann, S. K. Friedlander and A. Schmidt-Ott, *Journal of Nanoparticle Research*, 2002, **4**, 499–509.

16 S. Amoruso, G. Ausanio, R. Bruzzese, M. Vitiello and X. Wang, *Physical Review B*, 2005, **71**, 033406.

17 O. Senkov, C. Woodward and D. Miracle, *JOM*, 2014, **66**, 2030–2042.

18 A. Zelenyuk, D. Imre, J. Wilson, Z. Zhang, J. Wang and K. Mueller, *Journal of the American Society for Mass Spectrometry*, 2015, **26**, 257–270.

19 K. J. Suski, D. M. Bell, M. K. Newburn, M. L. Alexander, D. Imre, D. W. Koppenaal and A. Zelenyuk, *Spectrochimica Acta Part B: Atomic Spectroscopy*, 2021, **179**, 106092.

20 E. J. Kautz, M. C. Phillps, A. Zelenyuk and S. S. Harilal, *Physics of Plasmas*, 2022, **29**, 053509.

21 S. S. Harilal, M. C. Phillips, D. H. Froula, K. K. Anoop, R. C. Issac and F. N. Beg, *Rev. Mod. Phys.*, 2022, **94**, 035002.

22 S. S. Harilal, B. E. Brumfield, B. D. Cannon and M. C. Phillips, *Analytical chemistry*, 2016, **88**, 2296–2302.

23 E. J. Kautz, D. Senor and S. S. Harilal, *Journal of Applied Physics*, 2021, **130**, 204901.

24 P. J. Skrodzki, M. Burger, I. Jovanovic, M. C. Phillips, B. E. Brumfield, J. Yeak and S. S. Harilal, *Phys. Plasmas*, 2019, **26**, 083508.

25 S. Irimiciuc, S. Gurlui, G. Bulai, P. Nica, M. Agop and C. Focsa, *Applied Surface Science*, 2017, **417**, 108–118.

26 R. W. B. Pearse, A. G. Gaydon, R. W. B. Pearse and A. G. Gaydon, *The identification of molecular spectra*, Chapman and Hall London, 1976, vol. 297.

27 A. Zelenyuk, D. Imre, Y. Cai, K. Mueller, Y. Han and P. Imrich, *International Journal of Mass Spectrometry*, 2006, **258**, 58–73.

28 K. Ashbee, R. E. Smallman and G. Williamson, *Proceedings of the Royal Society of London. Series A. Mathematical and Physical Sciences*, 1963, **276**, 542–552.

29 J. Li, J. Cho, J. Ding, H. Charalambous, S. Xue, H. Wang, X. L. Phuah, J. Jian, X. Wang, C. Ophus *et al.*, *Science advances*, 2019, **5**, eaaw5519.

30 E. J. Kautz, M. C. Phillips and S. S. Harilal, *Anal. Chem.*, 2020, **92**, 13839–13846.

31 T. Tsuji, K. Iryo, N. Watanabe and M. Tsuji, *Applied surface science*, 2002, **202**, 80–85.

32 B. Tan and K. Venkatakrishnan, *Optics express*, 2009, **17**, 1064–1069.

33 M. W. Chase, *Journal of Physical and Chemical Reference Data*, 1996, **25**, 1069–1111.

34 R. Zhang, A. Khalizov, L. Wang, M. Hu and W. Xu, *Chemical reviews*, 2012, **112**, 1957–2011.

35 T. Seto, Y. Kawakami, N. Suzuki, M. Hirasawa, S. Kano, N. Aya, S. Sasaki and H. Shimura, *Journal of Nanoparticle Research*, 2001, **3**, 185–191.

36 S.-H. Kim, P. W. Kang, O. O. Park, J.-B. Seol, J.-P. Ahn, J. Y. Lee and P.-P. Choi, *Ultramicroscopy*, 2018, **190**, 30–38.

37 Y. Zhang, D. Zhang, J. Wu, Z. He and X. Deng, *AIP Advances*, 2017, **7**, 075010.

38 R. L. Penn and J. F. Banfield, *American Mineralogist*, 1998, **83**, 1077–1082.

39 Y. Yao, Q. Dong, A. Brozena, J. Luo, J. Miao, M. Chi, C. Wang, I. G. Kevrekidis, Z. J. Ren, J. Greeley *et al.*, *Science*, 2022, **376**, eabn3103.